Supplementary Information (SI) for Physical Chemistry Chemical Physics.
This journal is © the Owner Societies 2024

SUPPLEMENTARY INFORMATION

for

Dried Hybrid Imogolite Nanotubes as Solids with a Changeable Surface Area: An Insight into Textural Properties based on the Correlation between Nitrogen Gas Adsorption, Immersion Calorimetry into Water, and Small Angle X-ray Scattering

Ali Dhaini[1], Amine Geneste[1], Fadwa AlFadel Raad[2], Pierre Picot[2], Gaëlle Martin Gassin[1], Bénédicte Prelot[1], Pierre-Marie Gassin[1], Philippe Trens[1], Antoine Thill[2]*, Jerzy Zajac[1]*

[1] ICGM, UMR 5253, Univ. Montpellier, CNRS, ENSCM, Montpellier, France

[2] Université Paris-Saclay, CEA, CNRS, NIMBE, LIONS, 91191 Gif Sur Yvette, France

* Corresponding authors:

Jerzy Zajac (jerzy.zajac@umontpellier.fr), Antoine Thill (antoine.thill@cea.fr)

S.1. An overview of the previously published information about the specific surface area of imogolite samples

Table S1. *BET specific surface areas reported in the literature for various imogolite samples as a function of the type of the sample, the drying procedure, and the degassing temperature applied before the measurement of gaseous N_2 adsorption at 77 K*

IMO type	Drying procedure	Degassing temperature (K)								Ref
		423	473	498	523	548	573	773	Other	
		BET surface area ($m^2 \cdot g^{-1}$)								
Natural IMO-OH	Not mentioned		255	257	270	318				1
Synthetic IMO-OH			240	259	340	398				
Synthetic IMO-OH (50% Ge)				297	332	403				
Synthetic IMO-OH	Ambient drying at 323 K	213					362			2
Synthetic IMO-OH	Ambient drying at 323 K						362			3
Synthetic IMO-CH_3		357					740		280*	
Synthetic IMO-OH	Ambient drying at 323 K	213					362	197		4
Synthetic IMO-CH_3		357					740	530		
Synthetic IMO-OH	Not mentioned						352			5
Synthetic IMO-CH_3							665			
Synthetic IMO-OH	Ambient drying at 353 K								282**	6
Synthetic IMO-OH	Freeze drying				458					7
Synthetic IMO-CH_3	Not mentioned					615				8

* no degassing procedure applied ** temperature not mentioned

S2. Thermal stability studies of imogolite samples and efficiency of the dehydration procedures

Studies of thermal stability were conducted based on thermogravimetric (TG) and mass-spectrometry (TG-MS) analysis. The TG measurements were performed using a NETZSCH Jupiter STA 449 apparatus coupled with a mass spectrometry (MS) analyzer. The temperature calibration was carried out using an Al_2O_3 crucible. About 20 mg of the sample were placed in a programmable furnace within the apparatus and heated under argon from 300 to 850 K at 10 $K \cdot min^{-1}$. The mass spectra corresponding to m/z = 1, 2, 12, 15, 16, 17, 18, and 44 were recorded over the same temperature range. For a selected sample, the TG and MS curves have been plotted as a function of temperature in Figure S1.

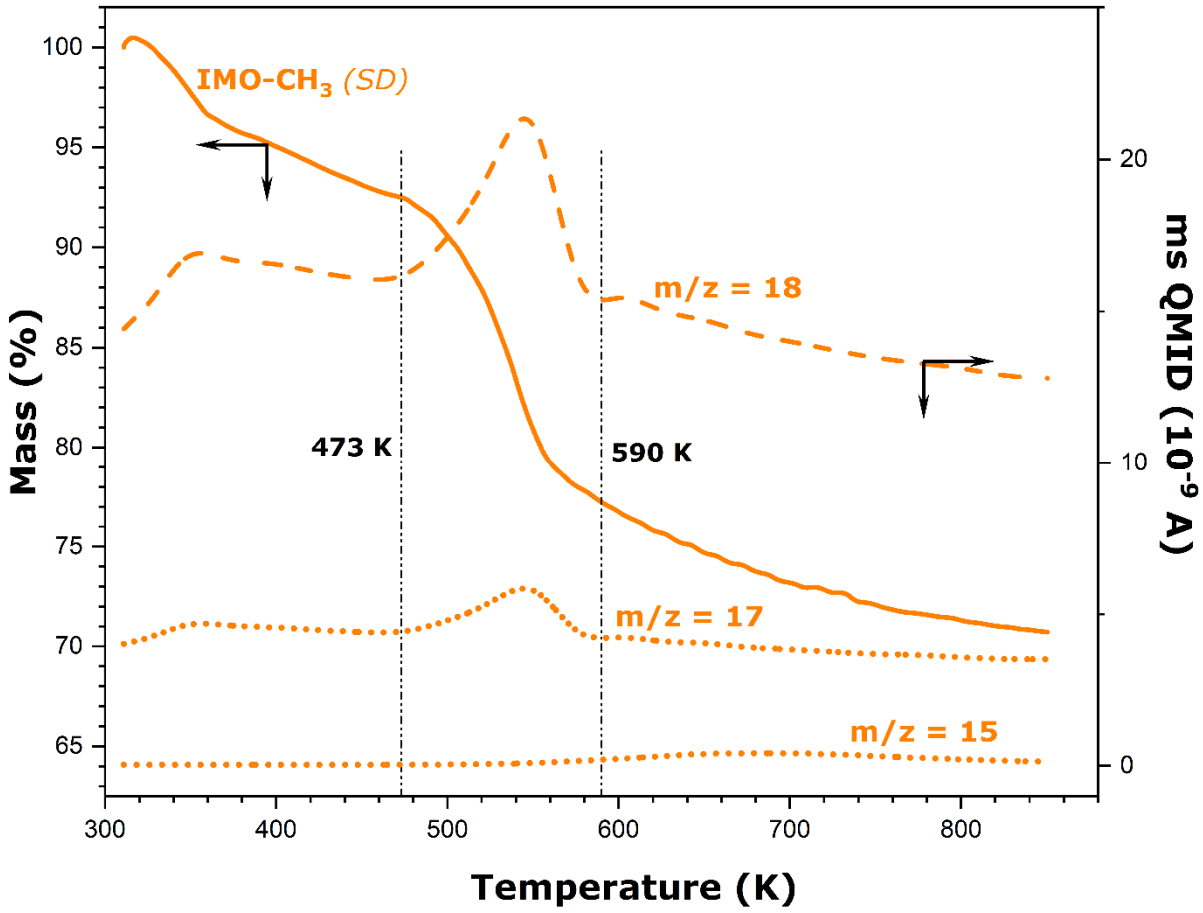

Figure S1. *TGA curve (solid line) and corresponding mass spectroscopy QMID (quasi multiple ion detection) ion current curves under argon flow for spray dried IMO-CH_3 in the temperature range of 300 – 850 K. The dashed and dotted lines represent the QMID curves corresponding to mass-to-charge ratios of 15, 17, and 18. For the other m/z values, the recorded changes in the QMID signal are too small to be of concern.*

Three domains of mass loss are observed in Figure S1, with clear breaks in the slope of the plot marking the change between these domains. The first region extends from 298 to 473 K and it can be ascribed to the removal of adsorbed water molecules from the accessible hydrophilic surface of nanotubes and, very probably, also from the inside of the nanotubes (pores A), as their inner walls are hydrophobic. The second region starts at about 473 K and continues up to about 590 K. It is likely attributable to further water removal from small inter-tube (type B) pores having hydrophilic walls, as well as the dehydroxylation of aluminol groups located mostly at the outer curved surfaces of IMO nanotubes. The departure of water molecules throughout the first two temperature ranges is well evidenced by the mass spectroscopy QMID curves, since the same trends are seen on the curves corresponding to mass-to-charge ratios of 17 and 18 [9]. The mass loss beyond 590 K is still accompanied by more continuous removal of water (m/z = 18) from the sample. Some degradation of the internal Si-CH_3 groups may be also postulated here, in line with small but noticeable changes in the m/z 15 QMID signal. It is thus clear that the thermal treatment under argon flow is not sufficient to completely eliminate water from the IMO-CH_3 sample. The most probable scenario is that water molecules retained within small inter-tube (type B) pores having hydrophilic walls are more difficult to be removed under such conditions. Nevertheless, it is not recommended to heat the sample to high temperatures since the gibbsite to boehmite phase transformation begins above 473 K [10]. Alternatively, the sample may be subjected to a vacuum treatment.

In the next step, the IMO-CH_3 materials underwent a simultaneous vacuum and thermal treatment. The presence of surface water was monitored *in situ* by FT-IR spectroscopy in the drift mode. The spectrometer (Bruker IFS 66 V) was equipped with a black body (global) source, a KBr splitter, and a mercury cadmium telluride (MCT) detector. The sample was prepared in the form of pellets by mixing 7 mg of IMO-CH_3 with 390 mg of KBr and pressing them under a pressure of 8 tons. A KBr reference pellet was prepared using 400 mg of pure KBr. The FT-IR study was made under a vacuum of 10^{-5} mbar and at different temperatures that were varied manually starting from 313 to 473 K by using a cryostat. Between two temperature steps, the sample was maintained for 10 min before recording the IR signal. At the end of each measurement series, the sample was degassed overnight at 473 K. The recordings were done in the mid-IR region (5000 – 400 cm^{-1}) with a spectral resolution of 4 cm^{-1} and a total of 64 scans. Figure S2 below presents the partial DRIFT spectra in a wavenumber region corresponding to water bending modes.

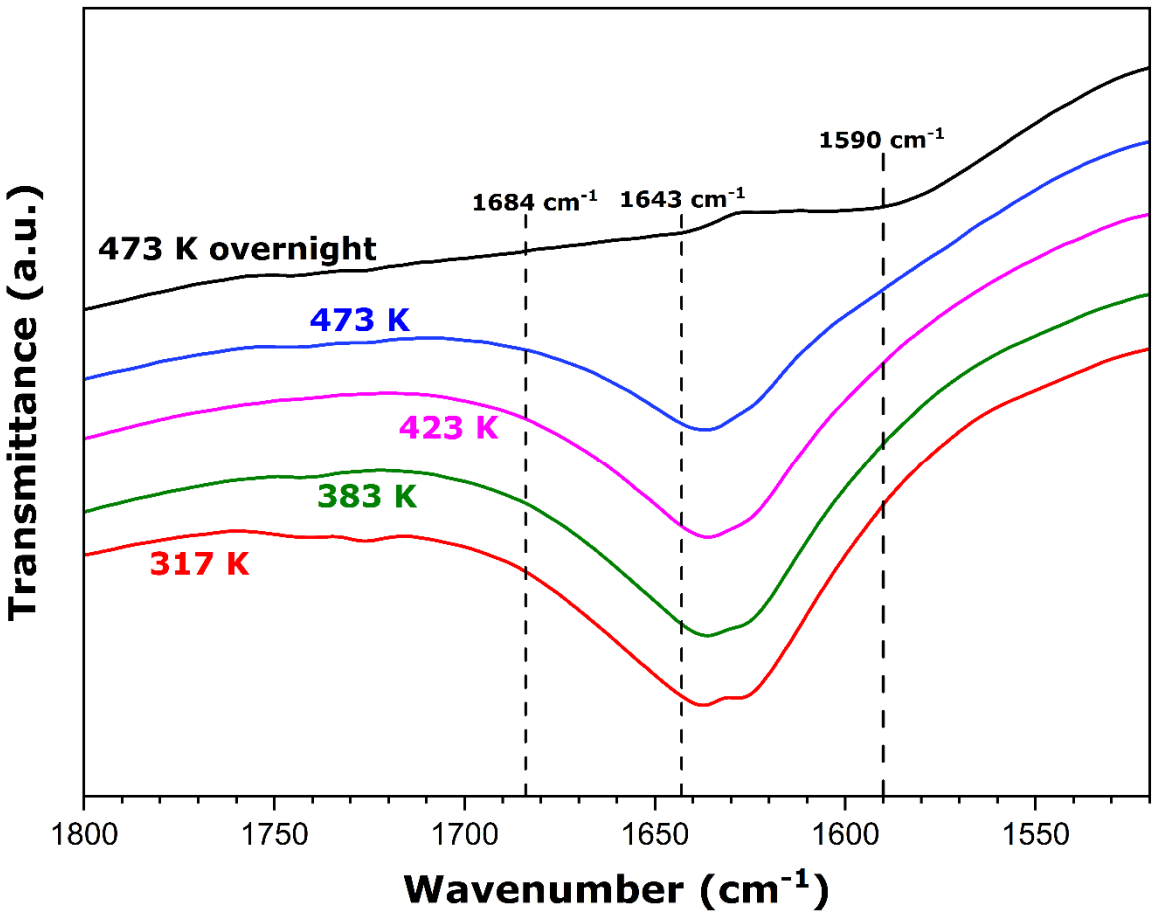

Figure S2. *DRIFT spectra of spray dried IMO-CH_3 recorded at different temperatures in the range corresponding to water bending modes.*

Two characteristic features at 1643 and 1590 cm^{-1} (marked by dashed lines in Figure S2) have been previously ascribed to the bending mode of water molecules and weakly H-bonded water inside the IMO-CH_3 nanotube; an additional feature at 1684 cm^{-1} corresponds to acid water [11]. The bands at 1684 and 1590 cm^{-1} do not appear on IR spectra of heated and shortly degassed samples. The peaks observed in the vicinity of 1643 cm^{-1} are mainly due to water molecules present on the external surface and between the tubes in the bundles. This component corresponding to the normal bending mode of water remains visible even until 473 K is reached. It becomes invisible in the scan obtained after overnight degassing at 473 K. This indicates that the removal of water from between the nanotubes is not fast and requires much time.

S3. Experimental and modeling SAXS studies on IMO nanotubes dispersed in water

The results of SAXS measurements made on IMO-OH and IMO-CH_3 nanotubes dispersed in water are presented in Figure S3. Since the nanotubes are not deformed upon dispersion in water, the analysis of the scattering signal allows the nanotube dimensions to be extracted with high precision.

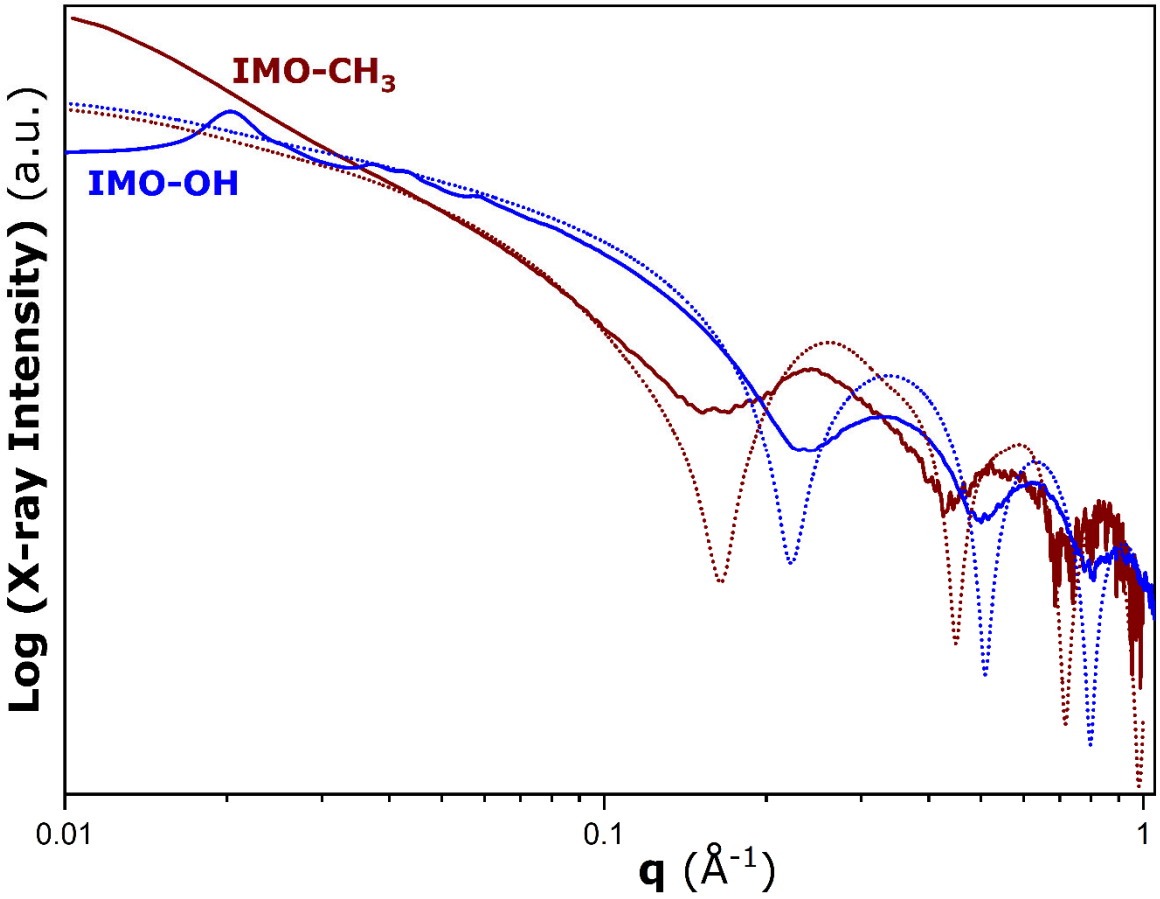

Figure S3. *Results of SAXS measurements made on IMO-OH (blue lines) and hybrid IMO-CH_3 (brown lines) nanotubes dispersed in water. The dotted lines correspond to the scattering of a model hollow cylinder having dimensions given further in Table 1.*

The molecular models of nanotubes were derived based on the (14,0) zig-zag structure for IMO-OH and the (9,9) one for IMO-CH_3 with a nanotube length being about 200 nm. The molecular structures were relaxed by using LAMMPS software. A NVT molecular dynamic simulation at 300 K, referring to simplified harmonic potentials to describe Si-O and Al-O stretching and O-Si-O and O-Al-O bending, was done for 1 ns. The stiffness and equilibrium distances of the harmonic stretching and bending potentials were taken from Thill *et al.* [12].

Using the relaxed molecular structures, it was possible to compute the distances from the tube axis and the radial position of the successive atomic layers. Therefore, from these positions, the electronic density of each layer and the average electronic density of the imogolite wall were computed. Then, the scattering signal could be easily modeled either by computing the scattered intensity based on the Debye formula and Debyer software [13] or by using a simple approximation of a homogeneous cylinder having an internal diameter r_{int}, a wall thickness, and a scattering length density contrast obtained from the imogolite composition. In the q range smaller than 1 $Å^{-1}$, the two methods gave almost exactly the same result. These parameters have been collected in Table S2 for both samples considered in the present section.

Note also that the scattering signals produced by models of monodispersed hollow cylinders of both types have been added to Figure S3.

Table S2. *Atomic layer positions and boundaries, as well as electronic densities as inferred from the relaxed molecular structures of IMO-OH and IMO-CH_3 nanotubes based on the analysis of the SAXS scattering data presented in Figure S3; O_{int} and O_{ext} indicate the internal and external layer of oxygen atoms, respectively.*

Sample	IMO-OH			IMO-CH_3		
Atomic layer	Position (Å)	Boundaries (Å)	Density ($e^{-}\cdot Å^3$)	Position (Å)	Boundaries (Å)	Density ($e^{-}\cdot Å^3$)
O_{int} or C	7.86	7.07 – 8.65	0.34	9.1	8.31 – 9.88	0.33
Si	9.45	8.65 – 9.75	0.73	10.67	9.88 – 10.96	0.71
O_b	10.04	9.75– 10.59	1.5	11.26	10.96 – 11.8	1.47
Al	11.3	10.59– 11.71	1.08	12.34	11.8 – 12.93	1.07
O_{ext}	12.3	11.71 – 12.89	0.88	13.52	12.93 – 14.11	0.87

Since the electronic density of bulk water is 0.33 $e^{-}\cdot Å^{-3}$, the internal oxygen layer in the case of IMO-OH may have no significant contrast with the internal water molecules. Therefore, the "visible" X-ray inner surface lies between the O_{int} and Si atomic layers. The tube can thus be modeled by a hollow cylinder having an inner radius of 8.65 Å and a thickness of 4.24 Å (12.89 Å – 8.65 Å). The corresponding scattering curve is plotted as dotted lines in Figure S3. However, the "real" inner surface for gas adsorption may not be exactly the same as the X-ray

one. It would be more rational to choose a radius slightly smaller than the O_{int} position for the reference surface of gas adsorption. A value of 7 Å has been used for example by Le Caër et al. [14]. Such value is 0.9 Å apart from the O_{int} atomic layer which seems reasonable when taking into account a typical O-H distance.

For IMO-CH_3, the internal cavity does not contain bulk water. The internal electronic density is therefore less than 0.33 $e^{-}\cdot Å^{-3}$. The value of the internal density has a strong influence on the position of the first minimum of the scattering curve [15]. Here a value of 0.05 $e^{-}\cdot Å^{-3}$ with an internal radius of 9.9 Å and a thickness of 4.2 Å (14.11 Å – 9.88 Å) allows the observed scattering shape to be adjusted [14]. As in the case of IMO-OH, the X-ray surface may not be appropriate for describing gas adsorption, and a value slightly smaller (9 Å) than the CH_3 position has to be chosen. This value corresponds to the position of the C atomic layer.

Interestingly, the above consideration confirms the smaller size of IMO-OH cylinders compared to that of IMO-CH_3 ones. This smaller diameter of IMO-OH has been previously explained by the formation of intramolecular hydrogen bonds between inner surface silanol groups [16]. It is also possible that a steric effect plays a non-negligible role in the structuring of IMO-CH_3 tubes due to the bulkier methyl groups. Furthermore, IMO-OH nanotubes appear very well dispersed in the liquid phase, whereas the IMO-CH_3 ones already form small bundles. These observations, previously documented by Boyer et al. [17], are confirmed by the deformation of the first oscillation at $q \sim 0.2$ $Å^{-1}$ and by the departure from a q^{-1} trend typical of isolated 1D nano objects at low angles. In the case of IMO-OH, additional peaks can be observed at low q values. They are related to the formation of a columnar liquid crystal with the nanotubes organized as a 2D hexagonal phase [18].

S4. Textural properties of IMO-samples

Based on the N_2 adsorption isotherms reported in Figure 3, the porosity may be evaluated by applying the models and procedures available in the literature. Given the shape of these adsorption curves, the imogolite samples studied are considered to be predominantly microporous. In consequence, the non-local density functional theory (NLDFT) models are most appropriate to determine the pore size distributions (PSD) from measured gas adsorption isotherms [19, 20]. The PSD curves obtained for IMO-CH_3 samples have been plotted in Figure S4.

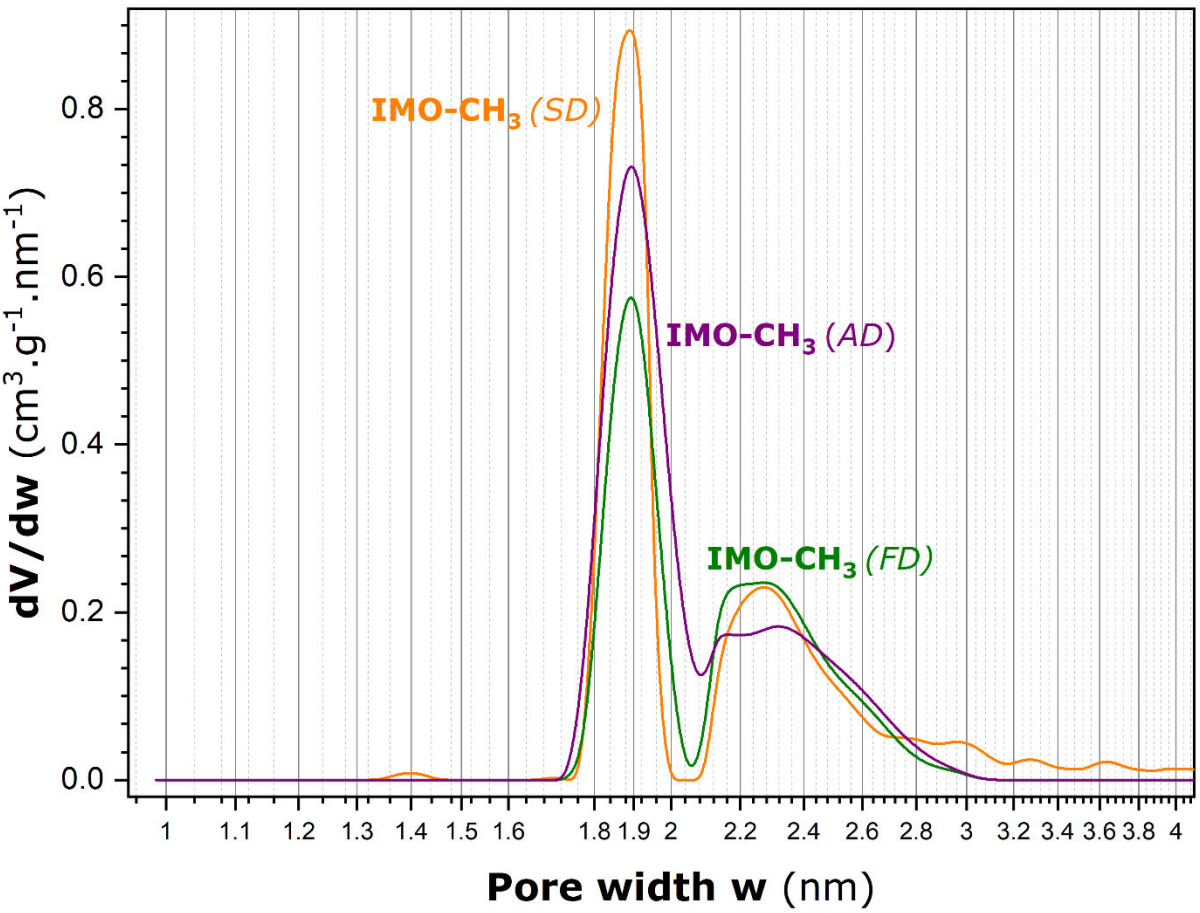

Figure S4. *Pore size distributions for IMO-CH₃ samples obtained by applying a DFT model available in Micromeritics software (cylindrical pores, oxide surfaces) to process the N₂ adsorption isotherms at 77 K.*

Two populations may be distinguished for each material, the first one is represented by a narrow high intensity peak centered at about 1.9 nm and the second one by a much broader low intensity peak. It is worthwhile noting that the most probable value of the first population is, within experimental error (1.9 ± 0.2 nm), equivalent to the inner cylinder diameter of IMO-CH₃ nanotubes, as inferred from SAXS measurements (Table 1). Since these nanotubes are not deformed upon drying, as demonstrated by SAXS studies, the first contribution to the pore volume should represent the porosity of type A. The second one could correspond to the porosity of type C. Stressing the broadness of the related PDS curve through the analysis of low angle part of the SAXS pattern in Figure 2 leads to the conclusion that inter-bundle pores are expected to be heterogeneous in size, depending on the long-range arrangement of the bundles.

In the case of IMO-CH₃ *(AD)* and IMO-CH₃ *(FD)*, the PSD plots are located in a narrow size range between 1.7 and 3 nm. On the contrary, IMO-CH₃ *(SD)* contains a small but non-

negligible quantity of mesopores larger than 2.7 nm, which may be responsible for the small hysteresis loop appearing on the adsorption-desorption isotherms (Figure 3).

To determine the total surface area and the volume of micropores, the adsorption isotherms measured for the reference gibbsite sample and three IMO materials have been processed based on the Brunauer–Emmett–Teller (BET) model for the multilayer adsorption and the t-plot procedure [21]. The equivalent specific surface area, S_{BET}, was calculated by taking the 0.162 nm^2 cross-sectional area for one adsorbed N_2 molecule as a rational approximation. The data processing procedure was adapted to describe solids possessing highly ordered pore structures. For this purpose, the BET model was applied in a particular p/p_0 interval, accounting for the presence of micropores in a given sample [21]. The volume of micropores, V_{mic}, was inferred from the intercept of the linear portion of the reduced adsorption isotherm (i.e., t-plot). The experimental isotherms reported in Figure 3 were transformed into corresponding t-plots (Figure S5) based on the Harkins–Jura equation for the universal curve describing the thickness of adsorbate layers on a non-porous surface as a function of relative pressures in the range between 0.1 and 0.75. Furthermore, the average surface area of micropores, S_{mic}, was calculated based on the model of cylindrical micropores by using the following formula $S_{mic} = \frac{4 \cdot V_{mic}}{d_{mic}}$, where V_{mic} is the result of the t-plot treatment and d_{mic} is identified with the pore width at which the PSD curves in Figure S4 take their maximum values (*i.e.*, 1.9 ± 0.2 nm).

The resulting S_{BET}, V_{mic}, and S_{mic} values have been collected in Table S3. Additionally, the best-fit value of the BET interaction constant, C_{BET}, is included in Table S3 to give an idea about the nature of porosity present in each sample.

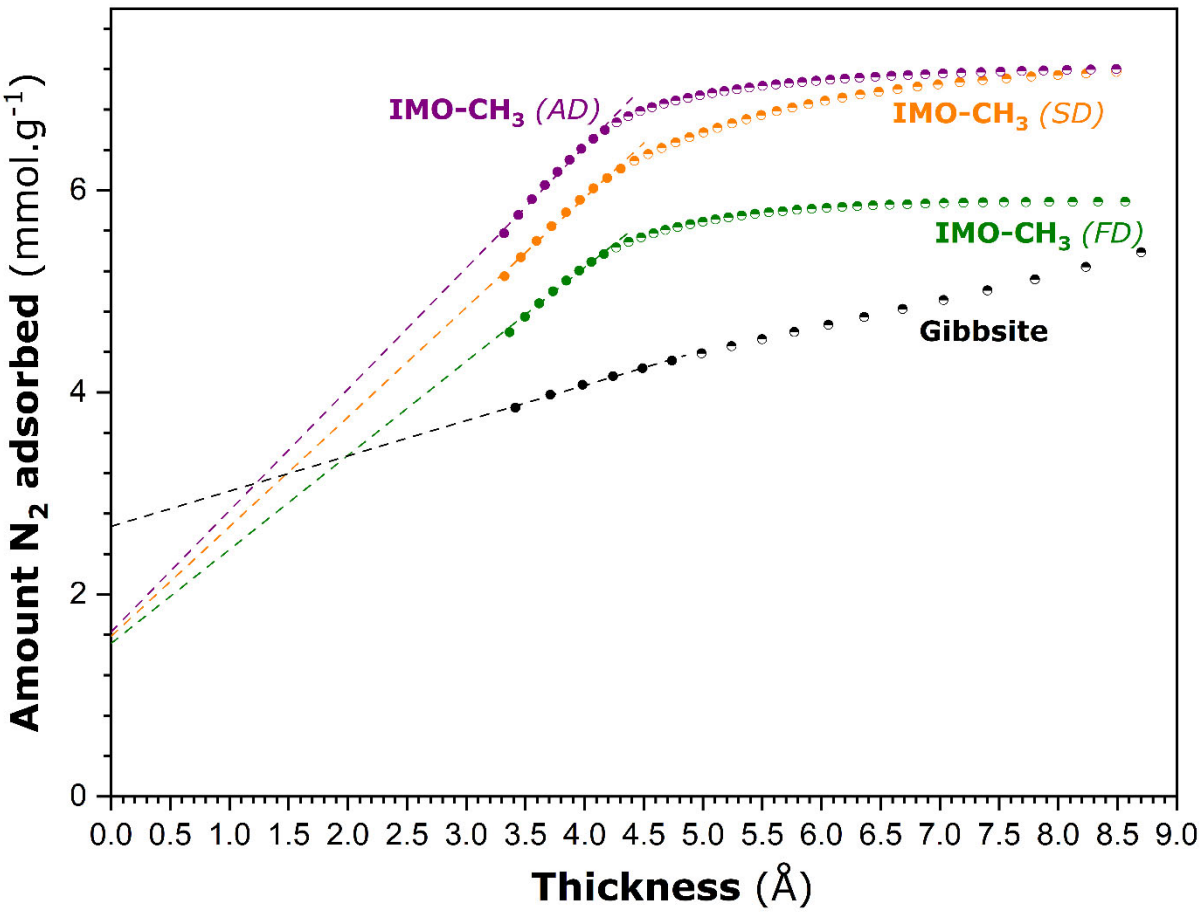

Figure S5. *t-plots constructed by means of Harkins–Jura equation from the experimental isotherms of N_2 adsorption onto gibbsite and IMO-CH_3 materials.*

Table S3. *Various specific surface area and porosity parameters, as determined by applying the BET model and t-plot procedure to analyze the N_2 adsorption isotherm for the reference gibbsite material, and imogolite samples. A more detailed explanation is given in the text.*

Method / Sample	BET		t-plot	Cylindrical pore
	S_{BET} ($m^2 \cdot g^{-1}$)	C_{BET}	V_{mic} ($cm^3 \cdot g^{-1}$)	S_{mic} ($m^2 \cdot g^{-1}$)
Gibbsite	355 ± 8	857 ± 18	0.093 ± 0.004	-
IMO-CH_3 *(SD)*	518 ± 13	168 ± 5	0.055 ± 0.004	117 ± 9
IMO-CH_3 *(AD)*	563 ± 12	163 ± 4	0.057 ± 0.005	120 ± 10
IMO-CH_3 *(FD)*	458 ± 16	163 ± 6	0.053 ± 0.004	112 ± 8

Concerning the C_{BET} constant, the three IMO-CH_3 materials cannot be regarded as fully microporous samples. It is interesting to note that the volume and surface area of micropores are far from the model value obtained based on SAXS measurements (Table 1). Moreover, the S_{mic} values are also much too small compared to the BET surface areas. Therefore, the classical t-plot procedure seems to fail to describe correctly the porosity of IMO samples. The main reason is that the pores of type A and C in the IMO-CH_3 samples represent a borderline between uniformly sized supermicropores and heterogeneous small mesopores. To better address this issue, the α_S-plot procedure is subsequently chosen because it does not depend on any *a priori* assumptions concerning the mechanism of adsorption by the reference material [21, 22]. It also allows the experimental adsorption isotherm to be transformed into an α_S-plot in a broader range of relative pressures from 0.001 to 0.9 [23]. The reduced adsorption isotherms for three IMO-CH_3 materials are shown in Figure S6.

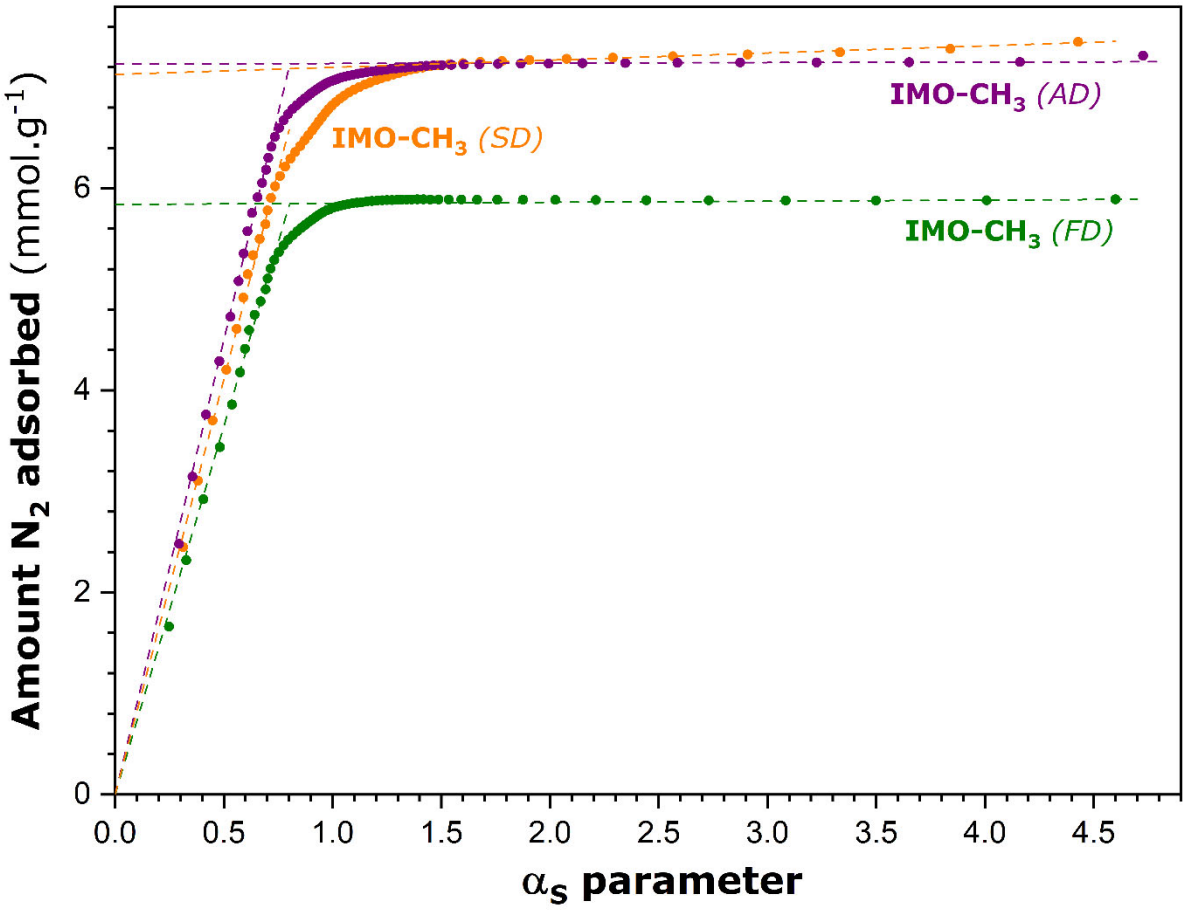

Figure S6. α_S*-plots obtained from the experimental isotherms of* N_2 *adsorption onto IMO-*CH_3 *materials. The experimental quantity of adsorption has been replotted against the reduced standard adsorption* α_S *measured on the reference non-porous adsorbent (non-porous silica).*

Note that the first linear portions of the α_S-plots always pass through the origin, which is characteristic mostly for the experimental adsorption isotherms of type II and IV (*i.e.*, non-porous, macroporous, and mesoporous adsorbents) but may also occur when the adsorption curve is of type Ib (adsorbents containing supermicropores) [21, 24]. In such a case, the total volume of pores, V_{pore}, present in each material is determined from the intercept of the last linear portion of the reduced adsorption isotherm in Figure S6. The slope of this straight line gives the external surface area, S_{ext}. The total surface area accessible to nitrogen, S_{tot}, is deduced from the slope of the first linear portion of the α_S-plot. The resulting parameters have been collected in Table S4.

Table S4. *Various specific surface areas and porosity parameters, as determined by applying the α_S-plot procedure to analyze the N_2 adsorption isotherm for the IMO-CH_3 imogolite samples.*

Parameter / Sample	S_{tot} ($m^2 \cdot g^{-1}$)	S_{ext} ($m^2 \cdot g^{-1}$)	V_{pore} ($cm^3 \cdot g^{-1}$)
IMO-CH_3 *(SD)*	533 ± 8	~ 5	0.25 ± 0.02
IMO-CH_3 *(AD)*	583 ± 6	~ 0	0.25 ± 0.03
IMO-CH_3 *(FD)*	472 ± 6	~ 0	0.21 ± 0.02

It is important to underline that the S_{tot} parameters are also close to the S_{BET} values reported in Table S3 for the three samples. The external surface areas are much smaller than the uncertainty in the surface area estimation. The S_{ext} parameter includes two major contributions: the lateral (base) surface area of IMO nanotubes as well as the outer curved surfaces of those nanotubes, which are located on the outer periphery of the bundles. The first contribution does not depend on the size of the bundles, but rather on the length of the constituent nanocylinders (c.f., section S5). The second contribution to S_{ext} depends strongly on the size of the bundles. In the case of large bundles, the number of nanotubes exposed on the periphery of each bundle is very small compared to those, which are packed in the bulk of the bundle (c.f., section S5). Since the external surface area for the IMO-CH_3 materials is only

of a few $m^2 \cdot g^{-1}$, the bundles existing in these samples appear as being composed of a large number of individual nanotubes, being rather a few hundreds of nanometers in length.

Since the α_S-plot method provides global information on the average porous structure, the S_{tot} and V_{pore} parameters may easily be considered reliable estimates of the porosity of type A and C in the dried IMO-CH_3 samples. The external surface area should be neglected in further consideration because of the magnitude of uncertainty in surface area determination.

S5. A simple geometric model to relate various surface areas to the number of nanotubes in a 2D hexagonal bundle.

To construct such a model, the following assumptions have been made:

1) The constituent nanotubes are not deformed (c.f., conclusions drawn from the SAXS studies).

2) They are organized on a perfect 2D hexagonal network.

3) The bundles are built by recursively adding a layer around the central nanotube.

4) The number of layers added is noted as n_C and the number of nanotubes in a bundle as N_C.

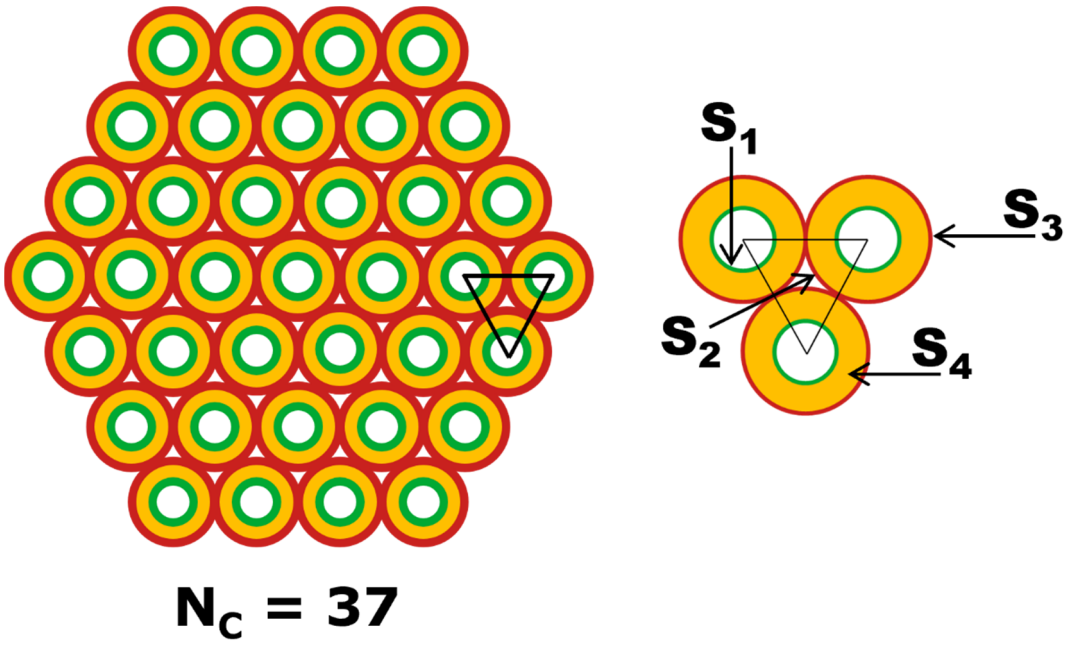

Figure S7. *Simple geometrical model of an imogolite bundle with a 2D hexagonal arrangement of 37 nanotubes in 3 layers around the central nanotube (left) and surface element of the bundle (right) showing the intra-tube surface area, S_1, the inter-tube surface area, S_2, the external curved surface area of the bundle, S_3, and the external base surface area, S_4.*

Figure S7 above illustrates various surface areas for a selected bundle containing 37 nanotubes (N_C = 37) ranged in 3 layers of nanotubes (n_C = 3) surrounding the central one. In line with the notation adopted in the main text, r_{inn}, r_{out}, V_{cyl}, and L_C denote, respectively, the inner radius, the outer radius, the volume, and the average length of the individual nanotube. The ratio between the radii of the outer, S_{out}, and the inner, S_{inn}, curved surfaces of the nanotubes is taken equal to 1.61 (Table 1). The S_{out} parameter is split into two area contributions being separated by the contact lines between the nanotubes at the external layer of the bundle: the external curved surface area of the bundle, S_3, and the inter-tube surface area, S_2, inaccessible to adsorbing N_2 molecules at 77 K.

The following geometrical relationships between the four surface areas, S_1, S_2, S_3, and S_4 may be deduced from the above model:

$$N_C = \left(\sum_{i=1}^{i=n_C} 6 \cdot i\right) + 1 \tag{S1}$$

$$S_1 = 2 \cdot \pi \cdot r_{inn} \cdot L_C \cdot N_C = N_C \cdot S_{inn} \tag{S2}$$

$$S_2 + S_3 = 2 \cdot \pi \cdot r_{out} \cdot L_C \cdot N_C = 1.61 \cdot N_C \cdot S_{inn} = 1.61 \cdot S_1 \tag{S3}$$

$$S_3 = 4 \cdot S_{out} + 3 \cdot (n_C - 1) \cdot S_{out} = 6.44 \cdot S_1 + 4.83 \cdot (n_C - 1) \cdot S_1 \tag{S4}$$

$$S_4 = 2 \cdot \pi \cdot (r_{out}^2 - r_{inn}^2) \cdot N_C = 2 \frac{V_{cyl}}{L_C} \left[\left(\frac{r_{out}}{r_{inn}}\right)^2 - 1\right] \cdot N_C = 3.18 \cdot \frac{V_{cyl}}{L_C} \cdot N_C \tag{S5}$$

Therefore, the intra-tube surface area, S_1, the inter-tube surface area, S_2, the external curved surface area of the bundle, S_3, and the external base surface area, S_4, may be evaluated as a function of the size of the bundle, N_C.

In an IMO-CH_3 sample dried in a given manner, the total number of non-deformed nanotubes per unit mass of the sample should *a priori* be constant and only the number of bundles may change, depending on the mutual arrangement and orientation of the nanotubes. In consequence, for a given intra-tube surface area, S_1, S_2, and S_3 parameters will depend on the drying procedure. **For further discussion, it is important to realize that S_1 and S_2 correspond well to the S_A and S_B parameters defined in the main text. On the contrary, the inter-bundle porosity of type C is not considered explicitly in the above model; in fact, the S_C area is included in the S_3 value together with the 'curved surface' component of the external surface area, S_{ext}, of the grains.**

To gain a more precise idea about the probable size of the bundles existing in each of the three IMO-CH_3 samples, the S_1 surface area will be taken as equal to 482 $m^2 \cdot g^{-1}$ in line with the geometrical parameter reported in Table 1 in the main text. The corresponding plots of S_2 and S_3 versus N_C are given in Figure S8.

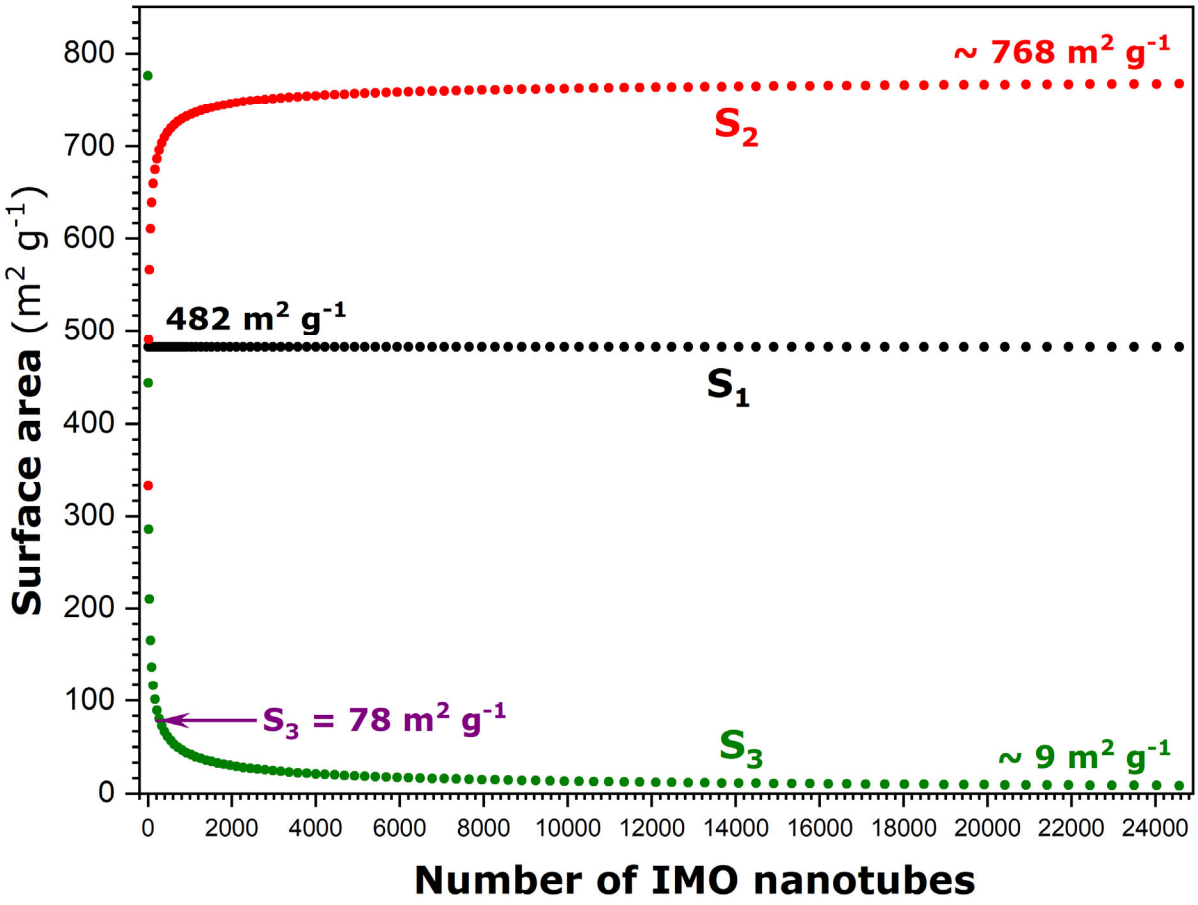

Figure S8. *Variations of the inter-tube surface area, S_2, and the external curved surface area, S_3, as a function of the total number of nanotubes in the sample, as predicted by the simple geometrical model presented in Figure S7. The intra-tube surface area, S_1, has been taken as being constant and equal to 482 $m^2 \cdot g^{-1}$ in consistency with the value obtained for spray dried IMO-CH_3 sample based on the SAXS measurements. A particular S_3 value of 78 $m^2 \cdot g^{-1}$ is marked by an arrow to complement the discussion in section 3.5 in the main text.*

It is clear that both surface parameters undergo opposite trends with increasing size of the bundles. The inter-tube surface area, S_2, increases very quickly to about 768 $m^2 \cdot g^{-1}$. Just the opposite, the area of the outer curved surfaces of those nanotubes, which are located on the outer periphery of the bundles shows a quick decay to about 9 $m^2 \cdot g^{-1}$. In addition, the S_4 area

can be assessed when putting into eq S5 the value of $V_{cyl} \cdot N_C$ from Table 1 in the main text (i.e., 0.22 $cm^3 \cdot g^{-1}$). When one considers that the length of IMO nanotubes, L_C, ranges between 100 and 1,000 nm [25], this lateral surface area extends between about 0.7 and 7 $m^2 \cdot g^{-1}$. These two estimates illustrate well the conclusion that the external surface area of large bundles is indeed very small.

S6. Effect of degassing temperature on the specific surface area and the enthalpy of immersion into water.

Table S3. *BET specific surface area and enthalpy of immersion into water for various IMO-CH_3 samples studied measured by varying the degassing temperature applied before the adsorption and calorimetry measurements.*

Sample	Degassing temperature (K)			Degassing temperature (K)		
	383	423	473	383	423	473
	S_{BET} ($m^2 \cdot g^{-1}$)			$\Delta_{imm}H$ ($J \cdot g^{-1}$)		
IMO-CH_3 *(SD)*	494 ± 20	500 ± 20	518 ± 13	-125 ± 6	-139 ± 6	-160 ± 7
IMO-CH_3 *(AD)*	533 ± 21	549 ± 22	563 ± 12	-121 ± 5	-139 ± 6	-153 ± 7
IMO-CH_3 *(FD)*	383 ± 15	411 ± 16	458 ± 16	-117 ± 5	-132 ± 6	-143 ± 6

References

1. W. C. Ackerman, D. M. Smith, J. C. Huling, Y. W. Kim, J. K. Bailey and C. J. Brinker, *Langmuir*, 1993, **9**, 1051-1057.
2. B. Bonelli, I. Bottero, N. Ballarini, S. Passeri, F. Cavani and E. Garrone, *J. Catal.*, 2009, **264**, 15-30.
3. I. Bottero, B. Bonelli, S. E. Ashbrook, P. A. Wright, W. Zhou, M. Tagliabue, M. Armandi and E. Garrone, *Phys. Chem. Chem. Phys.*, 2011, **13**, 744-750.
4. C. Zanzottera, A. Vicente, E. Celasco, C. Fernandez, E. Garrone and B. Bonelli, *J. Phys. Chem. C*, 2012, **116**, 7499-7506.
5. B. Bonelli, M. Armandi and E. Garrone, *Phys. Chem. Chem. Phys.*, 2013, **15**, 13381-13390.
6. T. Hongo, J. Sugiyama, A. Yamazaki and A. Yamasaki, *Nanopages*, 2013, **8**, 9-14.
7. P. Du, P. Yuan, A. Thill, F. Annabi-Bergaya, D. Liu and S. Wang, *Appl. Clay Sci.*, 2017, **150**, 115-124.
8. R. Nasi, F. Sannino, P. Picot, A. Thill, O. Oliviero, S. Esposito, M. Armandi and B. Bonelli, *Appl. Clay Sci.*, 2020, **186**, 105449.

9. Y. Liao, P. Picot, J.-B. Brubach, P. Roy, S. Le Caër and A. Thill, *Appl. Clay Sci.*, 2018, **164**, 58-67.
10. D. A. Ksenofontov and Y. K. Kabalov, *Inorg. Mater.*, 2012, **48**, 142-144.
11. Y. Liao, P. Picot, M. Lainé, J.-B. Brubach, P. Roy, A. Thill and S. Le Caër, *Nano Res.*, 2018, **11**, 4759-4773.
12. A. Thill, P. Picot and L. Belloni, *Appl. Clay Sci.*, 2017, **141**, 308-315.
13. M. Wojdyr, *Journal*.
14. S. Le Caer, M. C. Pignie, Q. Berrod, V. Grzimek, M. Russina, C. Carteret, A. Thill, J. M. Zanotti and J. Teixeira, *Nanoscale Adv.*, 2021, **3**, 789-799.
15. M. S. Amara, S. Rouzière, E. Paineau, M. Bacia-Verloop, A. Thill and P. Launois, *J. Phys. Chem. C*, 2014, **118**, 9299-9306.
16. S. U. Lee, Y. C. Choi, S. G. Youm and D. Sohn, *J. Phys. Chem. C*, 2011, **115**, 5226-5231.
17. M. Boyer, E. Paineau, M. Bacia-Verloop and A. Thill, *Appl. Clay Sci.*, 2014, **96**, 45-49.
18. E. Paineau, M.-E. M. Krapf, M.-S. Amara, N. V. Matskova, I. Dozov, S. Rouzière, A. Thill, P. Launois and P. Davidson, *Nat. Commun.*, 2016, **7**, 10271.
19. M. Thommes, K. Kaneko, A. V. Neimark, J. P. Olivier, F. Rodriguez-Reinoso, J. Rouquerol and K. S. W. Sing, *Pure Appl. Chem.*, 2015, **87**, 1051-1069.
20. P. I. Ravikovitch, G. L. Haller and A. V. Neimark, *Adv. Colloid Interface Sci.*, 1998, **76-77**, 203-226.
21. S. J. Gregg, Sing and K.S.W., *Adsorption, surface area and porosity*, Academic Press, London, 2nd edn., 1982.
22. J. Villarroel-Rocha, D. Barrera, A. A. G. Blanco, M. E. R. Jalil and K. Sapag, *Adsorpt. Sci. Technol.*, 2013, **31**, 165-183.
23. M. J. Meziani, J. Zajac, D. J. Jones, J. Rozière and S. Partyka, *Langmuir*, 1997, **13**, 5409-5417.
24. K. S. W. Sing and R. T. Williams, *Adsorpt. Sci. Technol.*, 2005, **23**, 839-853.
25. P. Picot, O. Taché, F. Malloggi, T. Coradin and A. Thill, *Faraday Discuss.*, 2016, **191**, 391-406.